Computation of the conducto-radiative effective heat conductivity of porous media defined by Triply Periodic Minimal Surfaces

Gerard Vignoles, Denis Rochais, Sylvain Chupin

Computation of the conducto-radiative effective heat conductivity of porous media defined by Triply Periodic Minimal Surfaces

Gerard L. Vignoles[a], Denis Rochais[b], Sylvain Chupin[b]

[a] *University of Bordeaux,*
Laboratory for ThermoStructural Composites (LCTS)
UMR 5801: CNRS-Safran-CEA-U. Bordeaux
3, Allée de La Boétie, 33600 Pessac, France
[b] *CEA, DAM, Le Ripault, BP 16, F-37260 Monts, France*

Abstract

Triply Periodic Minimal Surfaces are attractive porous media for the design of volumetric solar energy receivers ; their design involves the evaluation of their heat transfer capabilities in the mixed conductive/radiative mode. We present image-based computations of effective thermal conductivities (ETC) for different radiation/conduction ratios in twenty distinct TPMS structures, using a Hybrid Random Walk numerical method, considering Opaque/Transparent media. Results are cast in simple analytical correlations : the ETC is the sum of a purely conductive contribution proportional to the relative density and of a radiative contribution proportional to the radiation/conduction ratio; the coefficient of proportionality contains an emissivity-indepedent contribution and another contribution proportional to the emissivity which fades out above a critical ratio. This critical ratio is linearly proportional to the solid/void volume ratio of the media. These results are compared to similar ones obtained on open-cell foams. Application of these dimensionless laws to two realistic cases are presented as illustrative examples.

Keywords: TPMS; coupled heat transfer; radiation; effective conductivity; image-based modeling

Nomenclature

Symbol	Meaning	Unit
	Latin	
a_s	Solid thermal diffusivity	$m^2.s^{-1}$
d_p	Equivalent pore diameter	m
d_w	Equivalent wall thickness	m
E_R	Effective Rosseland emissivity	m^{-1}
k_s	Solid heat conductivity	$W.m^{-1}.K^{-1}$
k_{cond}	Heat conductivity linked to conduction only	$W.m^{-1}.K^{-1}$
k_{eff}	Effective heat conductivity	$W.m^{-1}.K^{-1}$
k^+	Radiative slope of conductivity *vs.* Nu'	-
k^+_∞	Purely radiative limit of k^+	-
k^+_R	Low-radiation value of k^+	-
$\tilde{k}$	Scaled heat conductivity	-
L	Image edge length	m
Nu'	Radiation/conduction ratio	-
Nu^*	Critical radiation/conduction ratio	-
S_V	Internal surface area per unit volume	m^{-1}
$\overline{T}$	Average temperature	K
t	Time	s
	Greek	
Δk^+	Slope of k^+ vs. emissivity at low Nu'	-
ε	Emissivity	-
Π	Pore volume fraction	-
ρ	Apparent specific mass	$kg.m^{-3}$
ρ_s	Solid phase specific mass	$kg.m^{-3}$
σ	Stefan's constant = $5.68 \cdot 10^{-8}$	$W.m^{-2}.K^{-4}$
τ	Thickness parameter	-
Φ	Solid volume fraction	-

1. Introduction

Volumetric solar energy receivers have recently received considerable attention due to their very high thermal conversion efficiency [1] as compared to tubular receivers [2]. For this high-temperature application (up to 1300 K) in corrosive environments, cellular ceramics are superior candidates, in particular SiC-based ones [3]. These high open porosity and specific surface materials are either monolithic honeycomb structures [4, 5], isotropic reticulated foams [4–10], non-extrudable 3D periodic lattices [7], or even multiscale structures [11]. The rapidly growing ability to prepare porous ceramic bodies by 3D printing methods [12] enables now a large wealth of achievable structures. Optimization of the architecture with respect to specified requirements may now include a numerical loop coupled to an experimental cycle. Structural optimization can be attempted through 3D numerical modeling of effective properties for variations of structural parameters, then by manufacturing the structures and verifying experimentally their increased performance [13]. In the case of heat transfer at high temperatures, this involves simulation of coupled heat transfer by conduction and radiation.

Among the numerous porous architectures that have been proposed for heat exchangers, Triply Periodic Minimal Surfaces (TPMS) [14, 15] have attracted special interest. Indeed, these surfaces, which have the peculiarity of having null Gaussian curvature everywhere [16], develop a very large surface-to-volume ratio, therefore increasing heat exchange between phases; they also can have pores under the form of somewhat tortuous channels, helping mixing of solutes in the fluid; finally they display very interesting mechanical properties such as strength-to-weight ratio [17]. This family of structures can be obtained by parametric equations describing a unit cell that can be repeated in the three spatial dimensions. It is therefore possible, through CAD and 3D printing techniques, to generate model materials with such structures, in which the geometrical surfaces are replaced by

walls with a specified thickness. The printed materials properties can be measured and compared to what can be computed in their numerical representations. An important foreseen application of TPMS is porous scaffolds for bone replacement, using calcium-phosphate-coated Ti6Al4V [18], putting focus on the evaluation of mechanical properties [17, 19–31] and on fluid permeability [15, 32]. Compressive [22, 31, 33–36], acoustic and energy absorption [37–42] properties have also been investigated. Another possible application is the preparation of support for heterogeneous catalysts [15, 43], in which the emphasis is set on the same properties, in addition to internal surface area and to heat conductivity.

Currently, to the authors' knowledge, heat transfer computations in TPMS porous structures [44, 45] have been restricted to conduction in the solid phase. In view of possible applications to Concentrated Solar Power volumic receivers, we propose in this paper, for the first time, a theoretical evaluation of conducto-radiative effective heat conductivity, considering them as Opaque/Transparent (OT) media. A recently developed software based on the principle of mixed random walks [46] allows the evaluation of such a property in 3D numerical representations of such media, as already proved on other cellular foams [47]. Here again, the objective is to link the thermal behavior of these porous media families to their geometrical properties, and to systematically predict the evolution trends of thermal conductivity with temperature for any member of the TPMS family.

In this paper, we will first describe the chosen numerical media and give a brief recall on the solution method, then present the results and discuss them.

2. Methods

2.1. Investigated numerical materials

Twenty numerical media deriving from TPMS were computer-generated and discretized. Four types have been chosen :

- The P type, for Schwartz's "Primitive" structure [23, 48]
- The D type, for Schwartz's "Diamond" structure[31]
- The G type, for "Gyroid" [22, 24, 27, 49]
- The I-WP type, for Schoen's "I-graph"-"Wrapped Package-graph" structure [21, 42]

Approximate equations [50] were used to produce the numerical representations. More precisely, first-order approximations were taken, *i.e.* only the leading term of the series development has been taken [51]. The equations are respectively the following:

Type	1^{st}-order approx. equation
$P:$	$P_\tau(x,y,z) = \cos x + \cos y + \cos z = \tau$
D:	$D_\tau(x,y,z) = \cos x \cos y \cos z - \sin x \sin y \sin z = \tau$
$G:$	$G_\tau(x,y,z) = \sin x \cos y + \sin z \cos x + \sin y \cos z = \tau$
$IWP:$	$IWP_\tau(x,y,z) = 2\,(\cos x \cos y + \cos z\, cosx + \cos y \cos z) - \ldots$
	$\ldots - (\cos 2x + \cos 2y + \cos 2z) = \tau$
$X^2:$	$(X_\tau(x,y,z))^2 = \tau$ where $X \in \{P, G, D, IWP\}$

Here, varying the τ parameter allows changing the relative dimensions of the two void subspaces separated by the walls. The square-power formula generates structure with a double wall. A constant wall thickness of 5 voxels has been chosen for all structures. All images were discretized in computation domains $200 \times 200 \times 200$ voxels in volume. The images were binarized and the solid/void interface was discretized with a Simplified Marching Cube scheme [52]. This technique allowed computing the relative density $\Phi = \rho/\rho_s$where ρ is the effective density of the structure and ρ_s the density of the bulk solid. Φ is also the solid

volume fraction and is related to the porosity Π by $\Phi = 1 - \Pi$. We also have computed the internal surface area S_V per unit volume and rough estimates of the effective pore hydraulic diameter $d_p = 4\Pi/S_V$ and of the strut diameter $d_s = 4\Phi/S_V$ which is defined in a similar way, inverting the roles of fluid and solid phases. The hydraulic diameter is defined as the ratio of the available volume to the wetted surface area [53]. All structures are described in Tables 1-4.

Preview Image	Function & para -meter	Relative density Φ (-)	Internal surf. area S_V (pix^{-1})	Effective strut diam. d_s (pix)	Effective pore diam. d_p (pix)	Void/solid ratio Π/Φ (-)
			P type			
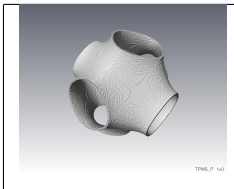	P_0	0.0575	0.0253	9.10	149.1	16.4
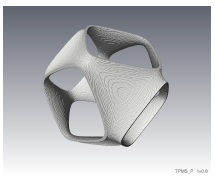	$P_{0.8}$	0.0541	0.0219	9.89	172.9	17.5
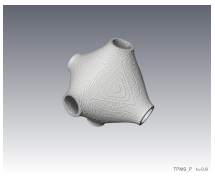	$P_{-0.8}$	0.0541	0.0219	9.89	172.9	17.5
			P^2 type			
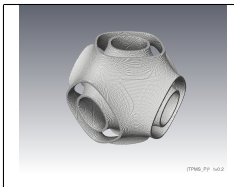	$P^2_{0.2}$	0.1174	0.0486	9.66	72.6	7.5
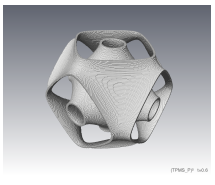	$P^2_{0.6}$	0.0962	0.0443	8.69	81.7	9.4

Table 1: List of produced geometries of the P and P^2 types.

Preview Image	Function & para -meter	Relative density Φ (-)	Internal surf. area S_V (pix^{-1})	Effective strut diam. d_s (pix)	Effective pore diam. d_p (pix)	Void/solid ratio Π/Φ (-)
			D type			
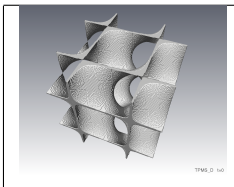	D_0	0.0983	0.0417	9.42	86.5	9.2
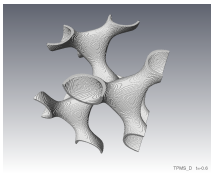	$D_{-0.6}$	0.0811	0.0299	10.83	122.7	11.3
			D^2 type			
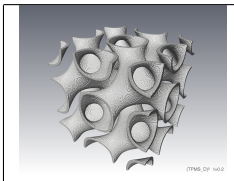	$D^2_{0.2}$	0.1898	0.0719	10.56	45.1	4.3
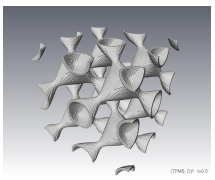	$D^2_{0.5}$	0.1120	0.0435	10.30	81.6	7.9

Table 2: List of produced geometries of the D and D^2 types.

Preview Image	Function & para -meter	Relative density Φ (-)	Internal surf. area S_V (pix^{-1})	Effective strut diam. d_s (pix)	Effective pore diam. d_p (pix)	Void/solid ratio Π/Φ (-)
			G type			
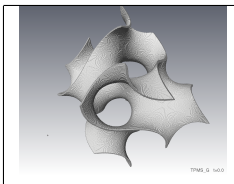	G_0	0.0713	0.0335	8.51	110.9	13.0
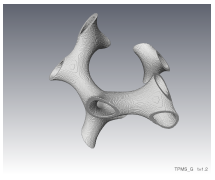	$G_{1.2}$	0.0545	0.0211	10.31	179.0	17.4
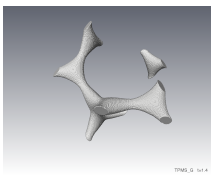	$G_{1.4}$	0.0381	0.00996	15.28	386.2	25.3
			G^2 type			
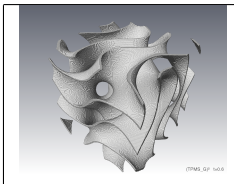	$G^2_{0.6}$	0.1174	0.0589	7.97	59.93	7.5
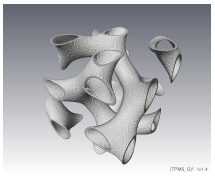	$G^2_{1.4}$	0.0854	0.0434	7.87	84.27	10.7
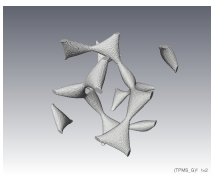	G^2_2	0.0426	0.0177	9.64	216.7	22.5

Table 3: List of produced geometries of the G and G^2 types.

Preview Image	Function & para -meter	Relative density Φ (-)	Internal surf. area S_V (pix^{-1})	Effective strut diam. d_s (pix)	Effective pore diam. d_p (pix)	Void/solid ratio Π/Φ (-)
			IWP type			
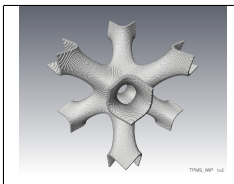	IWP_2	0.0739	0.0333	8.89	111.40	12.5
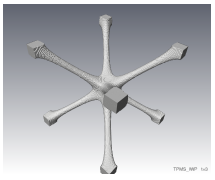	IWP_3	0.0470	0.0087	21.55	437.02	20.3
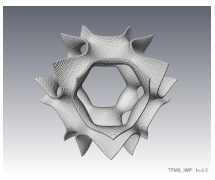	$IWP_{-2.5}$	0.0615	0.0292	8.43	128.64	15.3
			IWP^2 type			
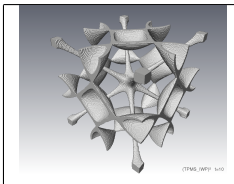	IWP^2_{10}	0.0859	0.0263	13.06	139.05	10.6
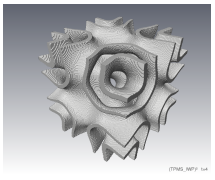	IWP^2_4	0.2620	0.0656	15.98	45.02	2.82

Table 4: List of produced geometries of the *IWP* and IWP^2 types.

2.2. Effective Thermal Conductivity (ETC) computations

Once the binarized image has been transformed into a biphasic resolution domain, the effective thermal diffusivity has been computed considering that the medium is Opaque/Transparent, *i.e.* the solid phase is purely conductive and the

void phase is perfectly transparent; we have used the Monte-Carlo Hybrid Random Walk scheme described in [46] and Einstein's formula. The method has been applied with 2000 random walkers, walking through the images during a dimensionless time $a_s t L^{-2} = 0.5$ (where a_s is the solid-phase thermal diffusivity and L the image edge size) using a "periodic+random tangential shift" boundary condition, so that the whole space is paved by repetitions of the image, and that the principal axes of the effective transfer are respected. The ETC is then obtained through multiplication by the heat capacity. Figure 1 is an example of random walker trajectory inside the discretized medium.

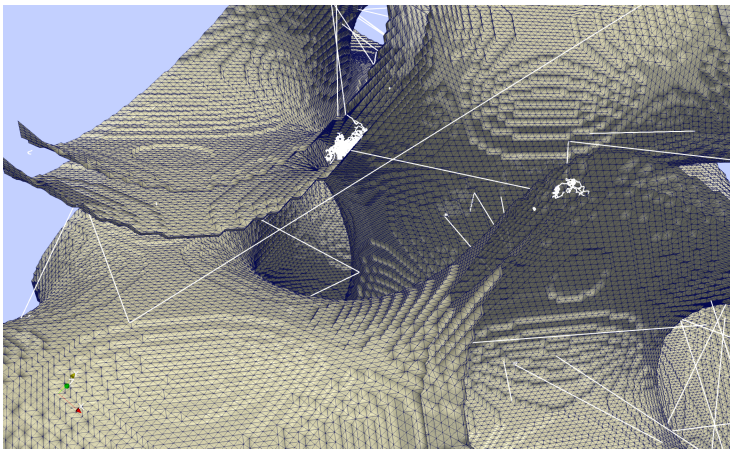

Figure 1: Example of a random walk in a TPMS structure discretized with the Simplified Marching Cube scheme. Walkers have a Brownian motion walk in the solid walls and propagate in straight segments between the walls.

Computations were carried out for varied values of the radiation/conduction ratio, conveniently described by the following dimensionless number [46]:

$$Nu' = \frac{4\sigma \overline{T}^3}{k_s} \frac{\Pi}{S_V} \tag{1}$$

where σ is Stefan's constant, $\overline{T}$ the average temperature of the medium (assuming temperature variations from one side to the other of the image is small with respect

to this average temperature), k_s the solid phase thermal conductivity, $\Pi = 1 - \Phi$ the pore volume fraction and S_V the internal surface area per unit volume. Note that Π/S_v is one-quarter of the equivalent pore diameter and is taken here as a reference length L_{ref}. This number can be understood as a scaled transfer coefficient. Indeed, the "equivalent radiative heat transfer coefficient" h_{rad} is equal to $4\sigma\overline{T}^3$. So, we can write $Nu' = \frac{h_{rad}L_{ref}}{k_s}$ as in a traditional Nusselt number. The ratio Nu' has been varied between 10^{-3} and 10^3 and the surface emissivity of the solid ε has been varied from 0.1 to 1.0, considering the solid as a grey, diffuse material.

3. Results

The ETC k_{eff} is rendered dimensionless by dividing it by the solid phase thermal conductivity k_s :

$$\tilde{k}_{eff} = k_{eff}/k_s \tag{2}$$

The typical accuracy of the computations was 4%, which suffices for the present purpose. Figure 2 is an example of the results obtained for various values of Nu' and ε. For $Nu' \rightarrow 0$, the ETC tends towards a limit k_{cond} which is linked to pure conduction through the solid phase ; it then increases with Nu', appreciably above 10^{-3}, to reach a common first-power dependency at high values irrespective of the value of ε. The intermediate regime shows dependency to the emissivity. Subtracting the purely conductive part to the ETC and dividing by Nu' gives a radiative slope :

$$k^+ = \left(\tilde{k}_{eff} - \tilde{k}_{cond}\right)/Nu' \tag{3}$$

This quantity has been plotted against Nu' for various emissivities in Figure 3, where the transition between both regimes clearly appears. All the points were

simultaneously fitted with the following relationship:

$$k^+ = k^+_\infty + \frac{\varepsilon \Delta k^+}{\frac{Nu'}{Nu^*} + 1} \tag{4}$$

where a critical value Nu^* appears. This value separates the domains for which radiation fully dominates conduction (for $Nu' > Nu^*$) and for which conduction still has an importance (for $Nu' < Nu^*$). As seen in Figure 3, the slope k^+ evolves between a high-temperature limit k^+_∞, independent of the emissivity, and a low-temperature limit ($k^+_\infty + \varepsilon \Delta k^+$). This behavior is exactly similar to the one observed in open-cell media [47]. When $Nu' < 10^{-1}$, which is usually the case, the Rosseland approximation is recovered :

$$\tilde{k}_{eff} \approx \tilde{k}_{cond} + \cdot Nu' \cdot \underbrace{(k^+_\infty + \varepsilon \Delta k^+)}_{k^+_R} \tag{5}$$

where $k^+_R = \frac{4}{3E_R}$ in which E_R is the classical Rosseland effective emissivity.

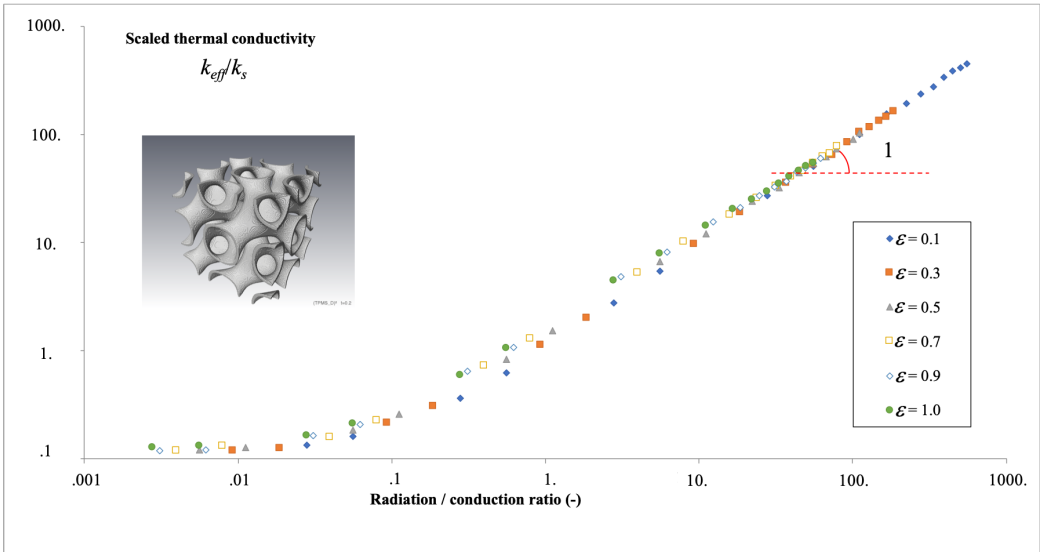

Figure 2: Scaled ETC as a function of the radiation/conduction ratio Nu' with various values of the emissivity ε for structure $D^2_{0.2}$.

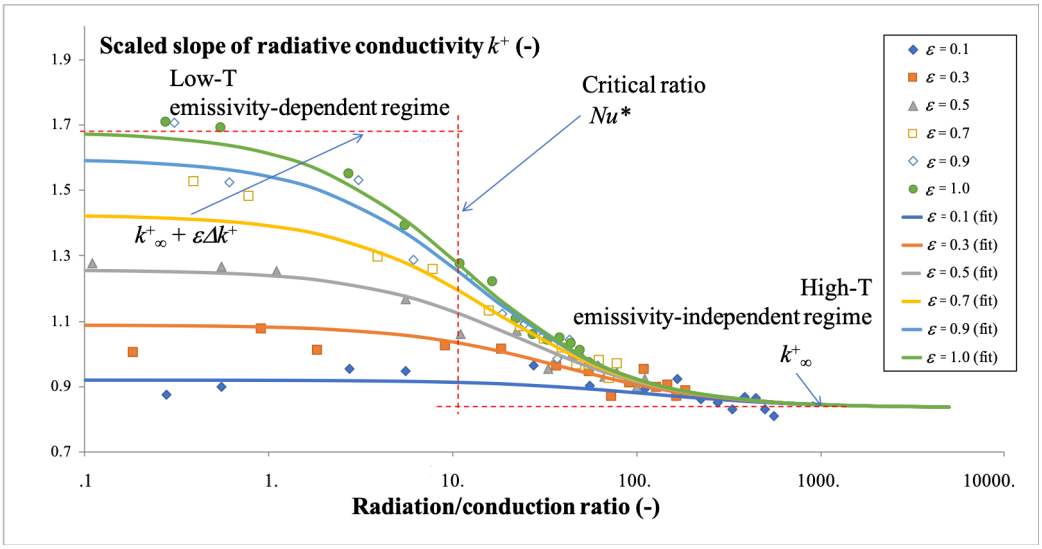

Figure 3: Scaled slope of the radiative part of the ETC k^+ as a function of the radiation/conduction ratio Nu' with various values of the emissivity ε for structure $D^2_{0.2}$.

The parameters $\tilde{k}_{cond}$, k_{∞}^{+}, Nu^{*} and Δk^{+} of (3) and (4) have been identified for all studied media. The results are reported in Table 5.

Function & para -meter	Scaled conductive contribution $\tilde{k}_{cond}/\Phi$	Radiative slope high-T limit k^{+}_{∞}	Emissivity-dependent slope increment Δk^{+}	Critical ratio Nu^{*}
P_0	0.61	0.894	1.030	30.15
$P_{0.8}$	0.61	1.026	0.989	33.25
$P_{-0.8}$	0.61	1.353	0.954	34.26
$P^2_{0.2}$	0.61	0.951	1.057	15.21
$P^2_{0.6}$	0.61	0.837	1.007	17.96
D_0	0.61	0.900	0.997	17.7
$D_{-0.6}$	0.61	1.608	1.013	20.6
$D^2_{0.2}$	0.61	0.835	0.845	11.7
$D^2_{0.5}$	0.59	1.443	0.907	17.0
G_0	0.61	0.956	0.980	25.7
$G_{1.2}$	0.61	1.934	0.983	32.8
$G_{1.4}$	0.61	2.013	0.818	58.5
$G^2_{0.6}$	0.61	0.985	0.912	14.3
$G^2_{1.4}$	0.61	1.531	0.940	21.2
G^2_2	0.61	2.151	0.933	31.9
IWP_2	0.61	1.300	1.024	24.3
IWP_3	0.61	1.502	0.704	59.3
$IWP_{-2.5}$	0.61	1.331	1.051	33.5
IWP^2_{10}	0.61	1.418	0.863	26.3
IWP^2_4	0.61	0.784	0.900	7.2

Table 5: Computed parameters describing the conducto-radiative ETC of all media using (3) and (4)

It has been found that, in all images, the scaled ETC in purely conductive regime is given by:

$$\tilde{k}_{cond} \approx 0.61\Phi \tag{6}$$

This factor is very close to the 2/3 factor given by Glicksman [54] and somewhat larger than the ones obtained in open-cell foams, which range from 0.4 to 0.55 [47]. The trend coincides almost exactly with the computations reported by Abueidda *et al.* [44] for all of his structures with cubic symmetry except gyroids (for which a 1/3 factor is reported). An experimental study [45] finds that the *G* type and other ones display the same correlation parameter, in apparent contradiction with [44].

The dimensionless parameters k_{∞}^{+} and Δk^{+} are close to unity, confirming the pertinence of the chosen scaling. Values are close to those obtained for open-cell foams [47], as illustrated in Figure 4. There seems to be a slight tendency for k_{∞}^{+} to increase when the relative density decreases, whereas no clear trend seems to appear for Δk^{+}. Note that it had been found that, in anisotropic media, the latter quantity is almost isotropic.

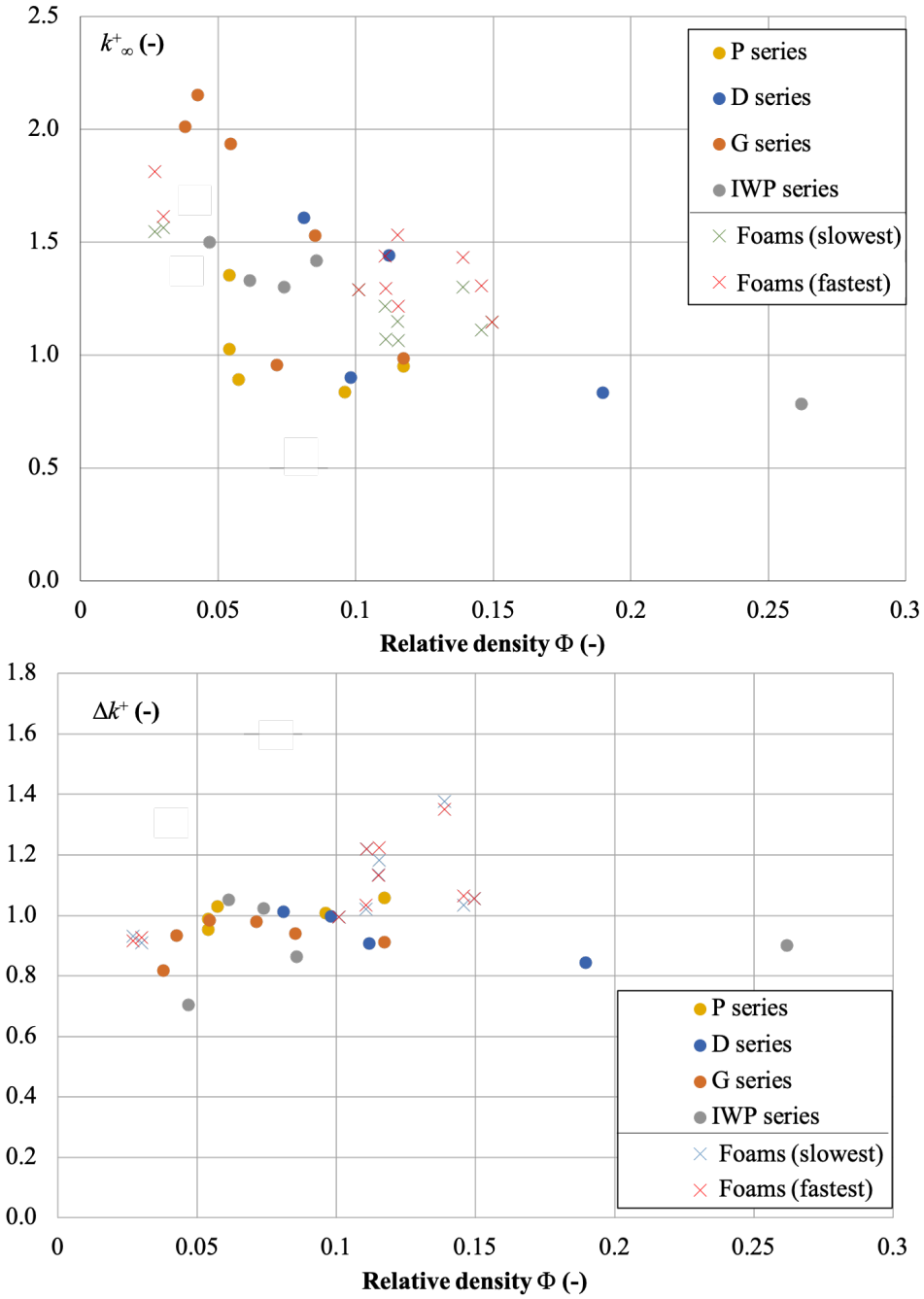

Figure 4: Parameters k^+_∞ (above) and Δk^+ (below) as a function of the relative density Φ.

Fig 5 is a plot of the obtained values of the critical ratio Nu^* *vs.* the void/solid ratio Π/Φ. There appears to be a rather clear scaling tendency, with $Nu^* \approx 2\Pi/\Phi$, as opposed to the tendency obtained previously on open-cell foams [47], which is $Nu^* \approx \Pi/\Phi$. This comes probably from the fact that the present TPMS structures are made of walls instead of struts.

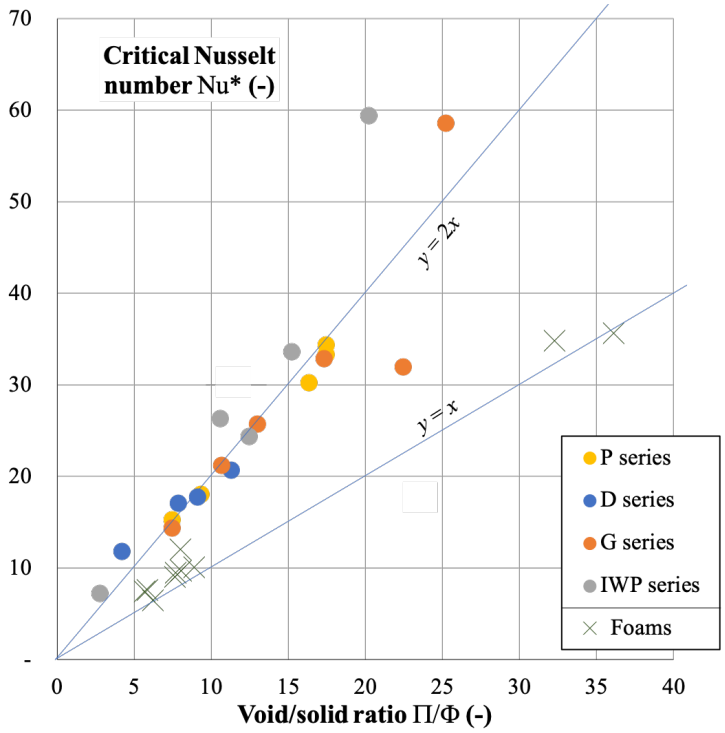

Figure 5: Critical ratio Nu^* as a function of the void/solid ratio Π/Φ for the TPMS models (circles), as compared to previous results obtained on open-cell foams [47] (crosses).

A physical justification for the correlations described in Fig. 5 could be given as follows, reminding that the modelled medium is OT. When Nu' becomes very high, most of the thermal gradient is captured inside the solid part of the material. Therefore, in this case, the precise value of the emissivity becomes pointless. On the other hand, when conduction dominates, most of the thermal gradient is con-

tained in the void part: in this case, it is sensitive to the value of the emissivity. Somehow, Nu^* translates a balanced situation between radiation and conduction, so it seems reasonable that it gets related to the volume ratio of conducting regions *vs.* radiating regions, which is Π/Φ. However, this type of relation is not expected to hold for closed-cell media, because in these media there is always a fully conductive path from one boundary of the medium to the other one, as is the case here, but on the other hand the void phase does not percolate from one side to the other; as a consequence, this changes the nature of the competition between conduction and radiation.

4. Examples of ETC predictions

To illustrate the potential interest of the presented computations, we present two examples of dimensional thermal conductivity predictions for ambient to high temperatures, using our dimensionless results and given data on the solid phase.

The first example is the $D^2_{0.2}$ structure made of sintered SiC, using a voxel edge size of 50 μm. The internal surface area is therefore 1437 m^{-1} and the effective pore diameter is 2.2 mm, the relative density being 19%. The solid phase intrinsic thermal conductivity k_s is retrieved from literature [55], and the emissivity is assumed constant: $\varepsilon = 0.85$. Figure 6 shows the evolution of the ETC with temperature up to 1700 K, above which SiC begins to creep. As the graph shows, the radiative contribution begins to be appreciable above 900 K and reaches $\approx 31\%$ at 1500 K, which is still modest.

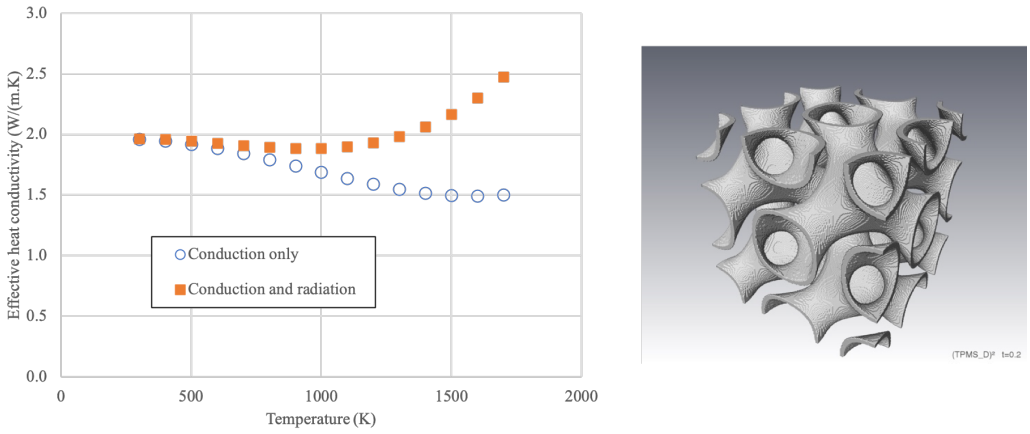

Figure 6: Predicted effective thermal conductivity of the example 1 structure (sintered SiC, 50 μm/voxel.

The second example is the $G_{1.4}$ structure made of Inconel 702 alloy, also using a voxel size of 50 μm. It is a very thin structure, with 4% solid phase only, the internal surface is 200 m^{-1} and the effective pore diameter is 19.2 mm. The solid phase conductivity has also been retrieved from literature [56] and the emissivity considered constant at 0.25. In Figure 7 we see that, as opposed to the first example, the radiative contribution to conductivity is already dominant above 500 K ; at 1300 K it represents 88% of the total effective conductivity, even though the surface emissivity of the solid is rather low. However, even in these conditions, the radiation/conduction ratio is only $Nu' \approx 10^{-1}$, so the transition to the emissivity-independent regime is never attained with realistic values of the temperature.

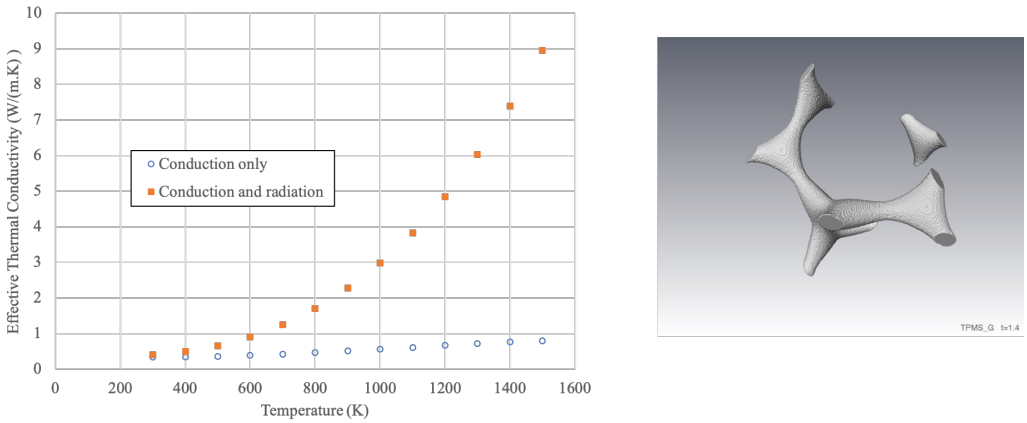

Figure 7: Predicted effective thermal conductivity of the example 2 structure (Inconel 702, 50 μm/voxel.

5. Conclusions and perspectives

In this document, we have reported image-based computations of effective thermal conductivities in the conducto-radiative regime for a variety of TPMS structures. The results are essentially in line with former results obtained on open-cell foams like Kelvin cell structures : (*i*) the Rosseland approximation for small temperature gradient holds, and the effective thermal conductivity is the sum of a conductive contribution and of a radiative contribution, (*ii*) the conductive contribution is proportional to relative density, (*iii*) the radiative contribution varies linearly with the radiation/conduction ratio and as an affine function of the surface emissivity at low temperatures, (*iv*) there is a transition towards a high-temperature regime in which the emissivity-dependent part of the radiative contribution disappears, (*v*) the critical ratio for this transition scales approximately as the double of the solid/void ratio, whereas it scales as the solid/void ratio itself in open-cell lattices. This last property arises probably from the fact that TPMS structures are made of walls instead of struts or beams.

Two examples of predictions of effective thermal conductivity *vs.* temperature are given, as an illustration of the potential use of the obtained results for the thermal design of media.

Perspectives of this work are the actual production of the designed media, followed by the measurement of their actual thermal properties, in order to check the consistency of such computations; this relies on independent measurements of the pure solid-phase conductivity. Actual design cases can be numerous, as can be understood from the two given examples.

Further work on conducto-radiative ETC computations is envisaged on other types of geometrical structures, either numerical, as is the case here, or actual (*e.g.* from CT scans). Another direction is the incorporation of convection in the porous media heat transfer simulations, so that a full design of a solar volumic receiver becomes feasible with a single piece of software.

References

References

[1] A. Kribus, Y. Gray, M. Grijnevich, G. Mittelman, S. Mey-Cloutier, C. Caliot, The promise and challenge of solar volumetric absorbers, Solar Energy 110 (2014) 463–481. doi:10.1016/j.solener.2014.09.035.

[2] D. Morris, A. López-Delgado, I. Padilla, M. Morris, Selection of high temperature materials for concentrated solar power systems: Property maps and experiments, Solar Energy 112 (2015) 246 – 258. doi:10.1016/j.solener.2014.09.050.

[3] S. Gianella, D. Gaia, A. Ortona, High Temperature Applications of Si-SiC Cellular Ceramics, Advanced Engineering Materials 14 (12, SI) (2012) 1074–1081. doi:10.1002/adem.201200012.

[4] T. Fend, High porosity materials as volumetric receivers for solar energetics, Optica Applicata 40 (2) (2010) 271–284.
URL http://opticaapplicata.pwr.edu.pl/files/pdf/2010/no2/optappl_4002p271.pdf

[5] S. Mey-Cloutier, C. Caliot, A. Kribus, Y. Gray, G. Flamant, Experimental study of ceramic foams used as high temperature volumetric solar absorber, Solar Energy 136 (2016) 226–235. doi:10.1016/j.solener.2016.06.066.

[6] T. Fend, B. Hoffschmidt, R. Pitz-Paal, O. Reutter, P. Rietbrock, Porous materials as open volumetric solar receivers: experimental determination of thermophysical and heat transfer properties, Energy 29 (2004) 823–833. doi:10.1016/S0360-5442(03)00188-9.

[7] T. Fend, R. Pitz-Paal, O. Reutter, J. O. Bauer, B. Hoffschmidt, Two novel high-porosity materials as volumetric receivers for concentrated solar radiation, Solar Energy Materials and Solar Cells 84 (1-4) (2004) 291 – 304. doi:10.1016/j.solmat.2004.01.039.

[8] Z. Wu, C. Caliot, F. Bai, G. Flamant, Z. Wang, J. Zhang, C. Tian, Experimental and numerical studies of the pressure drop in ceramic foams for volumetric solar receiver applications, Applied Energy 87 (2) (2010) 504–513. doi:10.1016/j.apenergy.2009.08.009.

[9] Z. Wu, C. Caliot, G. Flamant, Z. Wang, Coupled radiation and flow modeling in ceramic foam volumetric solar air receivers, Solar Energy 85 (9) (2011) 2374–2385. doi:10.1016/j.solener.2011.06.030.

[10] Z. Wu, C. Caliot, G. Flamant, Z. Wang, Numerical simulation of convective heat transfer between air flow and ceramic foams to optimise volumetric so-

lar air receiver performances, International Journal of Heat and Mass Transfer 54 (7-8) (2011) 1527–1537. doi:10.1016/j.ijheatmasstransfer.2010.11.037.

[11] A. Baux, L. Nouvian, K. Arnaud, S. Jacques, T. Piquero, D. Rochais, P. David, G. Chollon, Synthesis and properties of multiscale porosity ticsic ceramics, Journal of the European Ceramic Society 39 (8) (2019) 2601–2616. doi:10.1016/j.jeurceramsoc.2019.02.031.

[12] S. Chupin, D. Rochais, Y. Scaringella-Guerritat, From 3D images to 3D printed optimized materials for high insulation, in: E. Rank, F. Auricchio, P. Steinmann, S. Kollmannsberger (Eds.), Procs. Simulation for Additive Manufacturing 2017 (Sim-AM 2017), Vol. 2017-October, TU München, 2017, pp. 130–131.
URL https://www.scopus.com/inward/record.uri?eid=2-s2.0-85045523473&partnerID=40&md5=c38bf9afc927ac203edc503d699b20c4

[13] M. Pelanconi, M. Barbato, S. Zavattoni, G. Vignoles, A. Ortona, Thermal design, optimization and additive manufacturing of ceramic regular structures to maximize the radiative heat transfer, Materials and Design 163 (2019) 107539. doi:10.1016/j.matdes.2018.107539.

[14] S. Torquato, A. Donev, Minimal surfaces and multifunctionality, Proceedings of the Royal Society of London Series A: Mathematical, Physical and Engineering Sciences 460 (2047) (2004) 1849 – 1856. doi:10.1098/rspa.2003.1269.

[15] Y. Jung, S. Torquato, Fluid permeabilities of triply periodic minimal sur-

faces, Phys. Rev. E 72 (5) (2005) 056319. doi:10.1103/PhysRevE.72.056319.

[16] M. do Carmo, Differential Geometry of Curves and Surfaces, Prentice-Hall, Englewood Cliffs, NJ, 1976.

[17] O. Al-Ketan, M. Adel Assad, R. Abu Al-Rub, Mechanical properties of periodic interpenetrating phase composites with novel architected microstructures, Composite Structures 176 (2017) 9–19. doi:10.1016/j.compstruct.2017.05.026.

[18] J. Shi, L. Zhu, L. Li, Z. Li, J. Yang, X. Wang, A TPMS-based method for modeling porous scaffolds for bionic bone tissue engineering, Scientific Reports 8 (1) (2018) 7395. doi:10.1038/s41598-018-25750-9.

[19] O. Al-Ketan, M. Pelanconi, A. Ortona, R. Abu Al-Rub, Additive manufacturing of architected catalytic ceramic substrates based on triply periodic minimal surfaces, Journal of the American Ceramic Society 102 (10) (2019) 6176–6193. doi:10.1111/jace.16474.

[20] L.-Y. Zhu, L. Li, J.-P. Shi, Z.-A. Li, J.-Q. Yang, Mechanical characterization of 3D printed multi-morphology porous Ti6AL4V scaffolds based on triply periodic minimal surface architectures, American Journal of Translational Research 10 (11) (2018) 3443–3454.
URL https://europepmc.org/article/PMC/6291701

[21] O. Al-Ketan, R. Abu Al-Rub, R. Rowshan, The effect of architecture on the mechanical properties of cellular structures based on the IWP minimal surface, Journal of Materials Research 33 (3) (2018) 343–359. doi:10.1557/jmr.2018.1.

[22] L. Yang, C. Yan, W. Cao, Z. Liu, B. Song, S. Wen, C. Zhang, Y. Shi, S. Yang, Compression–compression fatigue behaviour of gyroid-type triply periodic minimal surface porous structures fabricated by selective laser melting, Acta Materialia 181 (2019) 49–66. doi:10.1016/j.actamat.2019.09.042.

[23] A. Z. Zabidi, S. Li, R. M. Felfel, K. G. Thomas, D. M. Grant, D. McNally, C. Scotchford, Computational mechanical characterization of geometrically transformed Schwarz P lattice tissue scaffolds fabricated via two photon polymerization (2PP), Additive Manufacturing 25 (2019) 399–411. doi:10.1016/j.addma.2018.11.021.

[24] E. Yang, M. Leary, B. Lozanovski, D. Downing, M. Mazur, A. Sarker, A. Khorasani, A. Jones, T. Maconachie, S. Bateman, M. Easton, M. Qian, P. Choong, M. Brandt, Effect of geometry on the mechanical properties of Ti-6Al-4V Gyroid structures fabricated via SLM: A numerical study, Materials and Design 184 (2019) 108165. doi:10.1016/j.matdes.2019.108165.

[25] R. Rahmani, M. Antonov, L. Kollo, Y. Holovenko, K. Prashanth, Mechanical behavior of Ti6Al4V scaffolds filled with $CaSiO_3$ for implant applications, Applied Sciences (Switzerland) 9 (18) (2019) 3844. doi:10.3390/app9183844.

[26] C. Bonatti, D. Mohr, Mechanical performance of additively-manufactured anisotropic and isotropic smooth shell-lattice materials: Simulations & experiments, Journal of the Mechanics and Physics of Solids 122 (2019) 1–26. doi:10.1016/j.jmps.2018.08.022.

[27] D. Abueidda, M. Elhebeary, C.-S. Shiang, S. Pang, R. Abu Al-Rub, I. Jasiuk, Mechanical properties of 3D printed polymeric Gyroid cellular structures:

Experimental and finite element study, Materials and Design 165. doi:10.1016/j.matdes.2019.107597.

[28] M. Sychov, L. Lebedev, A. Evstratov, A. Regazzi, J.-M. Lopez-Cuesta, Mechanical properties of cellular structures with Schwartz primitive topology, Lecture Notes in Networks and Systems 53 (2019) 80–86. doi:10.1007/978-3-319-99834-3_11.

[29] R. Ambu, A. Morabito, Modeling, assessment, and design of porous cells based on Schwartz primitive surface for bone scaffolds, Scientific World Journal 2019 (2019) 7060847. doi:10.1155/2019/7060847.

[30] Z. Cai, Z. Liu, X. Hu, H. Kuang, J. Zhai, The effect of porosity on the mechanical properties of 3D-printed triply periodic minimal surface (TPMS) bioscaffold, Bio-Design and Manufacturing 2 (4) (2019) 242–255. doi:10.1007/s42242-019-00054-7.

[31] J. Maszybrocka, B. Gapiński, M. Dworak, G. Skrabalak, A. Stwora, The manufacturability and compression properties of the Schwarz Diamond type Ti6Al4V cellular lattice fabricated by selective laser melting, International Journal of Advanced Manufacturing Technology 105 (7-8) (2019) 3411–3425. doi:10.1007/s00170-019-04422-6.

[32] D. Ali, M. Ozalp, S. B. G. Blanquer, S. Onel, Permeability and fluid flow-induced wall shear stress in bone scaffolds with TPMS and lattice architectures: A CFD analysis, European Journal of Mechanics, B/Fluids 79 (2020) 376–385. doi:10.1016/j.euromechflu.2019.09.015.

[33] M. Afshar, A. Pourkamali Anaraki, H. Montazerian, Compressive characteristics of radially graded porosity scaffolds architectured with mini-

mal surfaces, Materials Science and Engineering C 92 (2018) 254–267. doi:10.1016/j.msec.2018.06.051.

[34] H. Yin, Z. Liu, J. Dai, G. Wen, C. Zhang, Crushing behavior and optimization of sheet-based 3D periodic cellular structures, Composites Part B: Engineering 184 (2019) 107565. doi:10.1016/j.compositesb.2019.107565.

[35] M. Keshavarzan, M. Kadkhodaei, M. Badrossamay, M. Karamooz Ravari, Investigation on the failure mechanism of triply periodic minimal surface cellular structures fabricated by Vat photopolymerization additive manufacturing under compressive loadings, Mechanics of Materials 140 (2020) 103150. doi:10.1016/j.mechmat.2019.103150.

[36] L. Zhang, S. Feih, S. Daynes, S. Chang, M. Wang, J. Wei, W. Lu, Pseudo-ductile fracture of 3D printed alumina triply periodic minimal surface structures, Journal of the European Ceramic Society 40 (2) (2020) 408–416. doi:10.1016/j.jeurceramsoc.2019.09.048.

[37] K. Khan, R. Abu Al-Rub, Time dependent response of architectured Neovius foams, International Journal of Mechanical Sciences 126 (2017) 106–119. doi:10.1016/j.ijmecsci.2017.03.017.

[38] D. Abueidda, I. Jasiuk, N. Sobh, Acoustic band gaps and elastic stiffness of pmma cellular solids based on triply periodic minimal surfaces, Materials and Design 145 (2018) 20–27. doi:10.1016/j.matdes.2018.02.032.

[39] L. Zhang, S. Feih, S. Daynes, S. Chang, M. Wang, J. Wei, W. Lu, Energy absorption characteristics of metallic triply periodic minimal surface sheet structures under compressive loading, Additive Manufacturing 23 (2018) 505–515. doi:10.1016/j.addma.2018.08.007.

[40] M. Sychov, L. Lebedev, S. Dyachenko, L. Nefedova, Mechanical properties of energy-absorbing structures with triply periodic minimal surface topology, Acta Astronautica 150 (2018) 81–84. doi:10.1016/j.actaastro.2017.12.034.

[41] K. Khan, R. Abu Al-Rub, Modeling time and frequency domain viscoelastic behavior of architectured foams, Journal of Engineering Mechanics 144 (6) (2018) 04018029. doi:10.1061/(ASCE)EM.1943-7889.0001448.

[42] K. Khan, R. Abu Al-Rub, Viscoelastic properties of architected foams based on the Schoen IWP triply periodic minimal surface, Mechanics of Advanced Materials and Structures (2018), *in press*. doi:10.1080/15376494.2018.1538470.

[43] M. Lee, J. Lee, S. Han, K. Kang, Mechanical analyses of "shellular", an ultralow-density material, Acta Materialia 103 (2016) 595–607. doi:10.1016/j.actamat.2015.10.040.

[44] D. W. Abueidda, R. K. Abu Al-Rub, A. S. Dalaq, D.-W. Lee, K. A. Khan, I. Jasiuk, Effective conductivities and elastic moduli of novel foams with triply periodic minimal surfaces, Mechanics of Materials 95 (2016) 102–115. doi:10.1016/j.mechmat.2016.01.004.

[45] S. Catchpole-Smith, R. Sélo, A. Davis, I. Ashcroft, C. Tuck, A. Clare, Thermal conductivity of TPMS lattice structures manufactured via laser powder bed fusion, Additive Manufacturing 30 (2019) 100846. doi:10.1016/j.addma.2019.100846.

[46] G. L. Vignoles, A hybrid random walk method for the simulation of coupled conduction and linearized radiation transfer at local scale in porous media

with opaque solid phases, Int J Heat Mass Transfer 93 (2016) 707—719. doi:10.1016/j.ijheatmasstransfer.2015.10.056.

[47] G. L. Vignoles, A. Ortona, Numerical study of effective heat conductivities of foams by coupled conduction and radiation, International Journal of Thermal Sciences 109 (2016) 270–278. doi:10.1016/j.ijthermalsci.2016.06.013.

[48] D.-W. Lee, K. Khan, R. Abu Al-Rub, Stiffness and yield strength of architectured foams based on the Schwarz Primitive triply periodic minimal surface, International Journal of Plasticity 95 (2017) 1–20. doi:10.1016/j.ijplas.2017.03.005.

[49] A. Castro, R. Ruben, S. Gonçalves, J. Pinheiro, J. Guedes, P. Fernandes, Numerical and experimental evaluation of TPMS gyroid scaffolds for bone tissue engineering, Computer Methods in Biomechanics and Biomedical Engineering 22 (6) (2019) 567–573. doi:10.1080/10255842.2019.1569638.

[50] P. J. Gandy, S. Bardhan, A. L. Mackay, J. Klinowski, Nodal surface approximations to the P, G, D and I-WP triply periodic minimal surfaces, Chemical Physics Letters 336 (2001) 187–195. doi:10.1016/S0009-2614(00)01418-4.

[51] H. G. von Schnering, R. Nesper, Nodal surfaces of Fourier series: Fundamental invariants of structured matter, Zeitschrift für Physik B Condensed Matter 83 (3) (1991) 407–412. doi:10.1007/BF01313411.

[52] G. L. Vignoles, M. Donias, C. Mulat, C. Germain, J.-F. Delesse, Simplified marching cubes: An efficient discretization scheme for simulations of deposition/ablation in complex media, Computational Materials Science 50 (3)

(2011) 893 – 902. doi:http://dx.doi.org/10.1016/j.commatsci.2010.10.027.

[53] Frank M. White. *Fluid Mechanics*. McGraw-Hill, New York, NY, 8th edition, 2016. ISBN: 978-0-07-339827-3.

[54] L. Glicksman, M. A. Schuetz, Heat transfer in foams, in: N. C. Hilyard, A. Cunningham (Eds.), Low Density Cellular Plastics, Springer Netherlands, Dordrecht, 1994, pp. 105–152. doi:10.1007/978-94-011-1256-7.

[55] Y. S. Touloukian, Thermophysical Properties of High Temperature Solid Materials, MacMillan Co, New York, 1967.

[56] D. R. Flynn, Thermal conductivity of semiconductive solids : method for steady-state measurements on small disk reference samples, Interim Report 7740, Nat. Bureau of Standards, Washington, DC (1962).